The Astrophysical Journal, 953:169 (15pp), 2023 August 20 https://doi.org/10.3847/1538-4357/ace33f

Testing the Collisionless Nature of Dark Matter with the Radial Acceleration Relation in Galaxy Clusters

Sut-Ieng Tam[1], Keiichi Umetsu[1], Andrew Robertson[2], and Ian G. McCarthy[3]
[1] Academia Sinica Institute of Astronomy and Astrophysics (ASIAA), No.1, Sec. 4, Roosevelt Road, Taipei 10617, Taiwan; sitam@asiaa.sinica.edu.tw
[2] Jet Propulsion Laboratory, California Institute of Technology, 4800 Oak Grove Drive, Pasadena, CA 91109, USA
[3] Astrophysics Research Institute, Liverpool John Moores University, 146 Brownlow Hill, Liverpool L5 3RF, UK
Received 2022 June 27; revised 2023 June 27; accepted 2023 June 29; published 2023 August 16

Abstract

The radial acceleration relation (RAR) represents a tight empirical relation between the inferred total and baryonic centripetal accelerations, $g_{\rm tot} = GM_{\rm tot}(< r)/r^2$ and $g_{\rm bar} = GM_{\rm bar}(< r)/r^2$, observed in galaxies and galaxy clusters. The tight correlation between these two quantities can provide insight into the nature of dark matter. Here we use BAHAMAS, a state-of-the-art suite of cosmological hydrodynamical simulations, to characterize the RAR in cluster-scale halos for both cold and collisionless dark matter (CDM) and self-interacting dark matter (SIDM) models. SIDM halos generally have reduced central dark matter densities, which reduces the total acceleration in the central region when compared with CDM. We compare the RARs in galaxy clusters simulated with different dark matter models to the RAR inferred from CLASH observations. Our comparison shows that the cluster-scale RAR in the CDM model provides an excellent match to the CLASH RAR obtained by Tian et al. including the high-acceleration regime probed by the brightest cluster galaxies (BCGs). By contrast, models with a larger SIDM cross section yield increasingly poorer matches to the CLASH RAR. Excluding the BCG regions results in a weaker but still competitive constraint on the SIDM cross section. Using the RAR data outside the central $r < 100$ kpc region, an SIDM model with $\sigma/m = 0.3$ cm^2 g^{-1} is disfavored at the 3.8σ level with respect to the CDM model. This study demonstrates the power of the cluster-scale RAR for testing the collisionless nature of dark matter.

Unified Astronomy Thesaurus concepts: Dark matter (353); Galaxy clusters (584); Gravitational lensing (670); Cosmology (343); Intracluster medium (858)

1. Introduction

Based on modern cosmological studies (e.g., Hinshaw et al. 2013), dark matter is known to be the dominant matter component in the Universe, while its nature is still a mystery. In the current concordance cosmological model, Λ cold dark matter (CDM), large-scale structures formed hierarchically, with dark matter halos growing through a series of mergers of smaller halos as well as accretion. This standard model provides a good description of the observed large-scale structure.

However, there are issues on smaller scales that are potentially challenging for the CDM model. For example, collisionless dark matter particles in CDM produce cuspy dark matter halos, where the density rises toward the halo center, which is inconsistent with the cored density profiles inferred for the halos hosting some dwarf galaxies. This is the so-called cusp–core problem (Flores & Primack 1994; Moore 1994).

Spergel & Steinhardt (2000) proposed a promising alternative to collisionless CDM, known as self-interacting dark matter (SIDM). SIDM was proposed to solve the small-scale problems with CDM, while preserving the successful predictions on large scales in the ΛCDM model. Elastic collisions of dark matter particles effectively smooth out the mass distribution at the center of halos, leading to a deviation from the cuspy density profile of CDM halos. In Figure 1, we compare the density profiles of cluster-scale halos for different matter components, shown separately for simulations with five different dark matter runs (for details, see Section 2). The figure shows that the central dark matter density decreases with increasing dark matter scattering cross section. The scattering rate of dark matter particles, Γ, is proportional to the local dark matter density $\rho_{\rm dm}(r)$, the dark matter scattering cross section σ, and the local velocity dispersion $v(r)$ of dark matter particles (Rocha et al. 2013):

$$\Gamma(r) \simeq \rho_{\rm dm}(r) v(r) \sigma/m, \quad (1)$$

where m is the mass of a dark matter particle. Therefore, with the highest $\rho_{\rm dm}$ and v, massive galaxy clusters are crucial laboratories in which to search for dark matter self-interactions.

Galaxy clusters are the most massive gravitationally bound structures resulting from the hierarchical formation process. About 85% of their mass content is invisible dark matter, with the remainder being baryons that are mostly in the form of X-ray-emitting hot gas. Since cluster properties depend on the growth of structure, they contain an abundance of cosmological and astrophysical information. Several characteristic features of galaxy clusters have been used to test dark matter models, such as the shapes of dark matter halos (e.g., Peter et al. 2013; Umetsu et al. 2018), offsets between dark matter and galaxies in merging systems (e.g., Harvey et al. 2015; Massey et al. 2018; Wittman et al. 2018), the wobbling of brightest central galaxies (Harvey et al. 2019), and the amount and lensing efficiency of dark matter substructures (e.g., Jauzac et al. 2016; Meneghetti et al. 2020; Tam et al. 2020).

In the ΛCDM model, dark matter has negligible interaction with baryons, except through gravity. However, tight relations between the distributions of dark matter and of baryonic matter

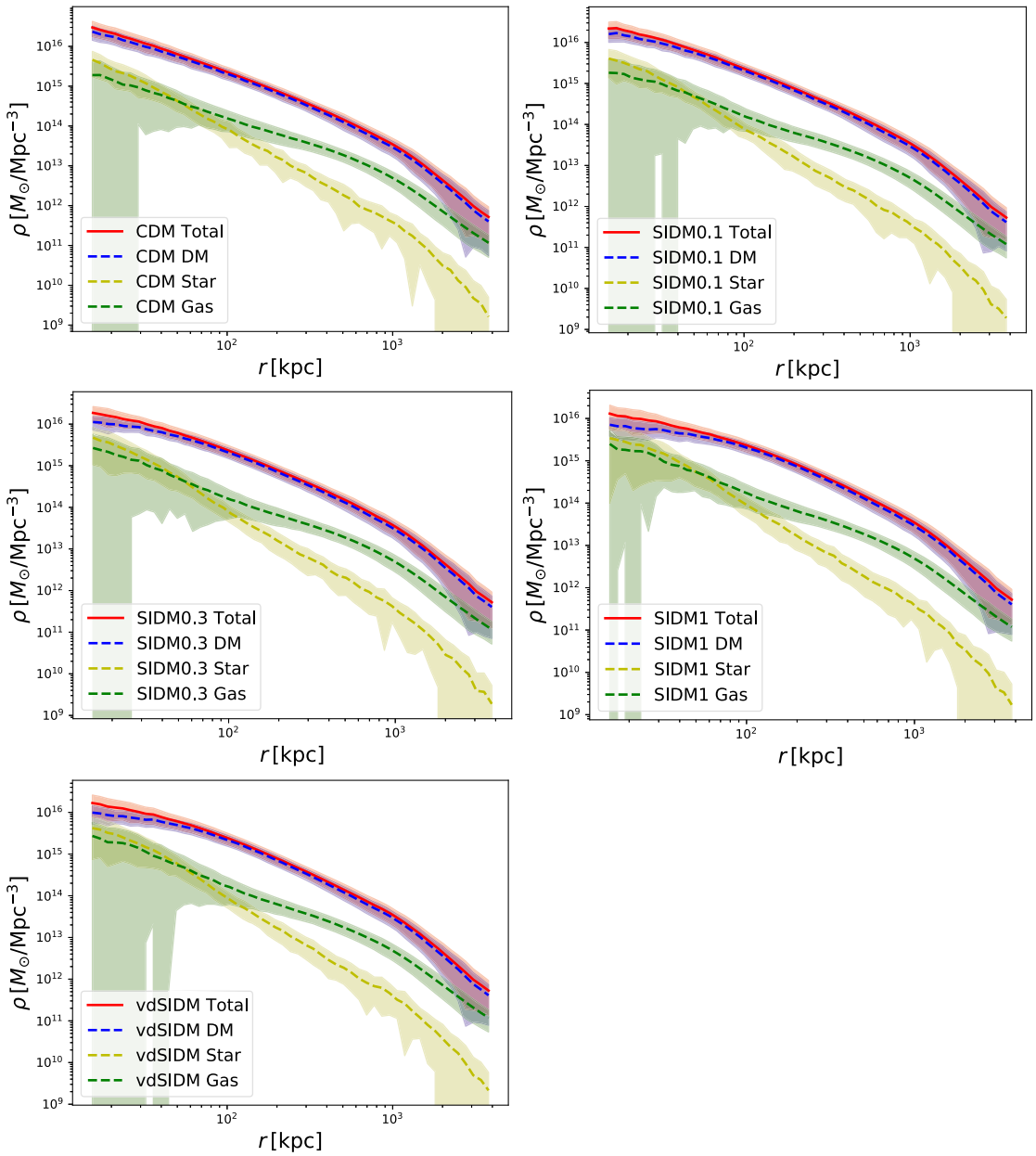

Figure 1. Mass density profiles for different matter components of cluster-scale halos with masses $E(z)M_{200} > 5 \times 10^{14}\ M_{\odot}$ at $z = 0.375$, shown for simulations with five different dark matter models. For each component, the dashed line represents the mean density profile and the shaded region shows the standard deviation around the mean profile. The large scatter in the innermost gas density is due to the feedback from active galactic nuclei in central galaxies, which removes most of the surrounding gas, thus leading to low central gas densities for some halos.

have been discovered. At the scale of spiral galaxies, the ratio of dynamical to baryonic masses, $M_{\rm tot}(<r)/M_{\rm bar}(<r)$, is found to be tightly coupled with gravitational acceleration, whereas no clear correlation with other physical quantities, such as galaxy size, has been found to date (McGaugh 2004).

By analyzing rotation curves of 153 spiral galaxies, McGaugh et al. (2016) found a tight correlation between two independent observables, namely the centripetal acceleration $g_{\rm tot}(r) = V^2/r = GM_{\rm tot}(<r)/r^2$ and the baryonic contribution to this acceleration $g_{\rm bar}(r) = GM_{\rm bar}(<r)/r^2$:

$$\frac{g_{\rm tot}}{g_{\rm bar}} = \frac{M_{\rm tot}}{M_{\rm bar}} = \frac{1}{1 - e^{-\sqrt{g_{\rm bar}/g_{\dagger}}}}, \tag{2}$$

characterized by a characteristic acceleration scale, $g_{\dagger} = (1.20 \pm 0.24) \times 10^{-10}$ m s^{-2}. This empirical relation between the total and baryonic centripetal accelerations is referred to as the radial acceleration relation (RAR). Since then, a much effort have been invested to study the RAR in various galaxy samples (e.g., Lelli et al. 2017; Rong et al. 2018; Chae et al. 2019; Oman et al. 2020; Brouwer et al. 2021). Hydrodynamical simulations in the ΛCDM framework have succeeded in reproducing the observed RAR of galaxies (e.g., Keller & Wadsley 2017; Ludlow et al. 2017; Garaldi et al. 2018; Dutton et al. 2019; Paranjape & Sheth 2021).

Recently, observational studies of the RAR have been extended to cluster-scale objects (e.g., Chan & Del Popolo 2020;

Tian et al. 2020; Pradyumna & Desai 2021; Pradyumna et al. 2021; Eckert et al. 2022a). Tian et al. (2020) studied the RAR for a subsample of 20 high-mass galaxy clusters targeted by the CLASH program (Postman et al. 2012). In their analysis, the total mass of each cluster is inferred from a combined analysis of strong- and weak-lensing data (Umetsu et al. 2016) and the baryonic mass from estimates of X-ray gas mass and stellar mass (Donahue et al. 2014). Chan & Del Popolo (2020) analyzed X-ray data for a sample of 52 non-cool-core clusters. They obtained the cluster RAR using X-ray hydrostatic estimates for the total mass and estimates of X-ray gas mass for the baryonic mass, ignoring the contribution of stellar mass to the baryonic component. Eckert et al. (2022a) studied the total and baryonic mass distributions for a sample of 12 X-COP clusters with observations of X-rays and the Sunyaev–Zel'dovich (SZ) effect, accounting for the contribution of stellar mass. They found a complex shape of the RAR that strongly departs from the RAR in galaxies.

All of these studies found that the characteristic acceleration scale $g_\dagger$ in clusters is about an order of magnitude larger than that obtained from galaxy-scale objects. Observational RAR studies have also been extended to group-scale objects. Gopika & Desai (2021) found that $g_\dagger$ of group-scale halos falls in between the values found for galaxies and for galaxy clusters. These observations suggest that there is no universal RAR that holds at all scales from galaxies to galaxy clusters.

Alternatively, the RAR observed at galaxy scales has been attributed to modified Newtonian dynamics (MOND; Milgrom 1983), which introduces a characteristic acceleration scale, $g_\dagger$, and modifies the dynamical law. However, MOND falls short in accounting for the total observed gravitational mass in galaxy clusters. For completeness it is worth mentioning other approaches to generalize the RAR to galaxy clusters, especially the eMOND framework of Zhao & Famaey (2012), where the parameter $g_\dagger$ is allowed to be a monotonically increasing function of the system's escape velocity such that $g_\dagger$ is several times greater in clusters than in field galaxies. Hodson & Zhao (2017) followed up this idea and presented fits to nearby relaxed clusters in the Chandra Sample (Vikhlinin et al. 2006). They succeed in this by tailoring $g_\dagger$ as a specific function of the Newtonian potential of the gas and the brightest cluster galaxies (BCGs; see their Equation (20) and their Figures A.1–A.11 for 20 galaxy clusters).

In this study, we use cosmological hydrodynamical simulations to study the RAR for simulated halos in both CDM and SIDM scenarios. We aim to explore a new method for constraining the collisionless nature of dark matter using the cluster-scale RAR, as well as to compare the RARs derived from numerical simulations with multiwavelength cluster observations.

This paper is organized as follows. Section 2 introduces the simulation data sets we use in this work. Section 3 shows the results of the halo RAR obtained from the simulations. Section 4 compares the theoretical predictions from the simulations with observational data from the CLASH program. In Section 5, we discuss the results and implications of our findings. Finally a summary is given in Section 6.

Throughout this paper, we assume a Wilkinson Microwave Anisotropy Probe (WMAP) 9 yr ΛCDM cosmology (Hinshaw et al. 2013) with $\Omega_{\rm m}=0.287$, $\Omega_\Lambda=0.713$, and a Hubble constant of $H_0=100h$ km s^{-1} Mpc^{-1} with $h=0.693$. We denote the critical density of the Universe at a particular redshift z as $\rho_{\rm c}(z)=3H^2(z)/(8\pi G)$ with $H(z)$ the Hubble function. We also define the dimensionless expansion function as $E(z)=H(z)/H_0$. We adopt the standard notation M_Δ to denote the total mass enclosed within a sphere of radius r_Δ within which the mean overdensity is $\Delta\times\rho_{\rm c}(z)$. We use "ln" to denote the natural logarithm.

2. Numerical Simulations

2.1. SIDM Models

In this work, we use simulations run with four different SIDM models, as well as CDM, that were presented in Robertson et al. (2019). Three of the SIDM models have velocity-independent cross sections with isotropic scattering of $\sigma/m=0.1$, 0.3, and 1 cm^2 g^{-1}, which we refer to as SIDM0.1, SIDM0.3, and SIDM1.0, respectively. The other SIDM model (hereafter vdSIDM) has a velocity-dependent and anisotropic cross section.

The vdSIDM differential cross section is (Robertson et al. 2017, 2021)

$$\frac{d\sigma}{d\Omega}=\frac{\sigma_0}{4\pi[1+(v^2/w^2)\sin^2(\theta/2)]^2}, \tag{3}$$

where w is a characteristic velocity below which the scattering is approximately isotropic with $\sigma=\sigma_0$. For collision velocities greater than w, scattering becomes anisotropic (favoring scattering by small angles) and the cross section decreases. Our vdSIDM model has $\sigma_0/m=3.04$ cm^2 g^{-1} and $w=560$ km s^{-1}, which was chosen to reproduce the best-fit cross section in Kaplinghat et al. (2016).

To understand the macroscopic behavior of anisotropic particle interactions, we can introduce the concept of momentum-transfer cross section for vdSIDM (e.g., Robertson et al. 2017, 2021):[4]

$$\sigma_T=2\int(1-|\cos\theta|)\frac{d\sigma}{d\Omega}d\Omega. \tag{4}$$

During collisions, the amount of momentum transferred in the direction of the collision is given as $\Delta p=p(1-\cos\theta)$ with a scattering angle of θ. When the velocity increases, the vdSIDM cross section becomes more anisotropic, favoring scatter by small angles. Therefore, to better describe the effects of an anisotropic cross section, σ_T gives more weight to larger angle scattering, which contributes a larger amount of momentum transfer, while it downweights the small-angle scatter. After integrating over the solid angle, we obtain the following expressions for the total cross section ($\sigma_{\rm tot}$) and the momentum-transfer cross section (σ_T):

$$\sigma_{\rm tot}(v)=\frac{\sigma_0}{1+v^2/w^2},$$
$$\sigma_T(v)=\sigma_0\frac{4w^4}{v^4}\left[2\ln\left(1+\frac{v^2}{2w^2}\right)-\ln\left(1+\frac{v^2}{w^2}\right)\right]. \tag{5}$$

For a massive cluster with $M_{200}=10^{15}\,M_\odot$ at $z=0$ and for a typical relative velocity between particle pairs of $\langle v_{\rm rel}\rangle\sim\sqrt{GM_{200}/r_{200}}$, we obtain $\sigma_{\rm tot}(\langle v_{\rm rel}\rangle)=0.40$ cm^2 g^{-1} and $\sigma_T(\langle v_{\rm rel}\rangle)=0.25$ cm^2 g^{-1} for our vdSIDM model. We refer

[4] In Robertson et al. (2017), σ_T is referred to as the modified momentum-transfer cross section and denoted as $\sigma_{\tilde{T}}$.

the reader to Robertson et al. (2021) for more details about the effective (velocity-averaged) cross section of vdSIDM halos.

2.2. BAHAMAS Simulations

We use *N*-body particle data from the Baryons and Haloes of Massive Systems (BAHAMAS) suite of cosmological hydrodynamical simulations (McCarthy et al. 2017, 2018) with WMAP 9 yr (Hinshaw et al. 2013) cosmology. BAHAMAS implements subgrid models for star formation and stellar and black hole feedback, and produces a good match to the observed stellar mass function, as well as the X-ray luminosities and gas mass fractions of galaxy groups/clusters. The simulations occupy large periodic boxes, $400h^{-1}$ Mpc on a side. For the SIDM simulations, we use the BAHAMAS-SIDM suite (Robertson et al. 2019), which used the same initial conditions and subgrid models as BAHAMAS, but included an implementation of dark matter scattering. The parameters associated with the galaxy formation physics used in BAHAMAS-SIDM were kept the same as for the original BAHAMAS-CDM simulation. The friends-of-friends algorithm (Davis et al. 1985) with a linking length of 0.2 times the mean interparticle separation was run on each $z = 0.375$ simulation output. From each simulation we extract the 10,000 most massive friends-of-friends groups, which have spherical-overdensity masses in the range $12.5 < \log_{10}[E(z)M_{200}/M_{\odot}] < 15.3$.

For each halo we calculate the total enclosed mass profile, as well as the enclosed mass profile of the baryons. The center of the halo is defined by the location of the most gravitationally bound particle, and the enclosed masses are calculated at 101 different radii, logarithmically spaced between proper (as opposed to comoving) lengths of 0.1 kpc and 4 Mpc. In addition, the total density as a function of radius is calculated by taking the difference in total enclosed mass at two successive radii and dividing by the volume of the associated spherical shell. We consider the geometric mean of the inner and outer shell radii to be the radius at which this density is calculated. This density profile for each halo was used to make Figure 1.

3. Characterization of the Cluster-scale RAR in the BAHAMAS Simulations

With the enclosed total and baryonic mass profiles $M_{\rm tot}(<r) = M_{\rm dm}(<r) + M_{\rm bar}(<r)$ and $M_{\rm bar}(<r)$ measured for each individual halo (Section 2.2), we calculate their total and baryonic centripetal acceleration profiles as

$$g_{\rm tot}(r) = \frac{GM_{\rm tot}(<r)}{r^2},$$
$$g_{\rm bar}(r) = \frac{GM_{\rm bar}(<r)}{r^2}. \quad (6)$$

Equation (6) should be regarded as the definition of $g_{\rm tot}(r)$ and $g_{\rm bar}(r)$, not the result of assuming spherical symmetry. In this section, we aim to characterize the relationship between $g_{\rm tot}$ and $g_{\rm bar}$ for samples of halos selected from the BAHAMAS-CDM and -SIDM runs, focusing on massive cluster-scale objects.

3.1. RARs in CDM and SIDM Halos

Figure 2 shows the joint distribution of baryonic and total centripetal accelerations ($g_{\rm bar}$, $g_{\rm tot}$) derived from a subsample of group- and cluster-scale halos at $z = 0.375$, with masses $E(z)M_{200} > 5 \times 10^{13}\ M_{\odot}$. The results are shown separately for the CDM and four different SIDM models. The halo centripetal accelerations are logarithmically sampled at scales from $r = 15$ kpc to $r = 4000$ kpc.

For each dark matter run, the magenta solid line represents the mean $g_{\rm tot}$ as a function of $g_{\rm bar}$, or the halo RAR. The yellow dashed line represents the expectation corresponding to the cosmic mean ratio of total to baryonic mass densities, $g_{\rm tot} = (\Omega_{\rm m}/\Omega_{\rm b})g_{\rm bar}$. In all cases, the RARs of simulated halos converge toward the cosmic mean, $g_{\rm tot}/g_{\rm bar} = \Omega_{\rm m}/\Omega_{\rm b}$, in the low-acceleration limit of $g_{\rm bar} \lesssim 10^{-13}$ m s^{-2}.

The red dashed line shows the McGaugh et al. (2016) relation (Equation (2)) observed in spiral galaxies over the acceleration range $-12 \lesssim \log_{10}(g_{\rm bar}/{\rm m\ s^{-2}}) \lesssim -9$. Overall, the RARs of our simulated sample have a normalization that is higher than that observed at galaxy scales (McGaugh et al. 2016), suggesting a higher contribution from dark matter at a given baryonic acceleration.

3.2. Mass Dependence of the Halo RAR

The full sample of 10,000 BAHAMAS simulated halos spans a wide range of halo mass. We therefore split our sample into three mass bins: $12.5 < \log_{10}[E(z)M_{200}/M_{\odot}] \leqslant 13.7$, $13.7 < \log_{10}[E(z)M_{200}/M_{\odot}] \leqslant 14.7$, and $\log_{10}[E(z)M_{200}/M_{\odot}] > 14.7$, to investigate the halo mass dependence of the RAR.

Figure 3 shows the resulting RARs in the three mass bins, for the five different dark matter models. For the lowest-mass bin, the RARs for different dark matter models largely overlap with each other, while for the highest-mass bin (corresponding to massive cluster halos) the slope of the RAR at high $g_{\rm bar}$ decreases with increasing SIDM cross section. The flattening feature in $g_{\rm tot}$ at high acceleration corresponds to the dark matter "cores" of approximately constant density at the center of SIDM halos. This distinguishing feature, being more significant in more massive halos, is consistent with the fact that the scattering rate is proportional to the local dark matter density and velocity dispersion (Equation (1)). This result indicates that the high-acceleration cluster-scale RAR can be used to probe the nature of dark matter. In the following analyses, we will focus on the 48 cluster-scale halos in the highest mass bin, which are more sensitive to the SIDM cross section.

The velocity dependence of the vdSIDM cross section is apparent in Figure 3. For high-mass halos, vdSIDM behaves most similarly to SIDM0.3, while for the group-scale halos, vdSIDM halos are most like SIDM1.0 halos. This behavior is consistent with Robertson et al. (2019; see their Figure 1) and reflects the fact that the vdSIDM cross section decreases with increasing relative velocity between dark matter particles, and relative velocities are larger in more massive halos.

In the above analyses, a minimum radius of $r = 15$ kpc is applied. From cluster observations, the enclosed mass in the inner regions $r \in [15, 100]$ kpc is difficult to measure. We therefore study the RARs for the same sets of halos discussed above, but with three larger minimum radii.

In Figure 4, we plot the RARs for the high-mass objects with radial cuts of $r_{\rm cut} = 15$ kpc, 58 kpc, 98 kpc, and 206 kpc. The radial cut of 98 kpc corresponds approximately to the regime of combined strong- and weak-lensing analyses, while a radial cut of 206 kpc represents the regime of weak-lensing-only analyses

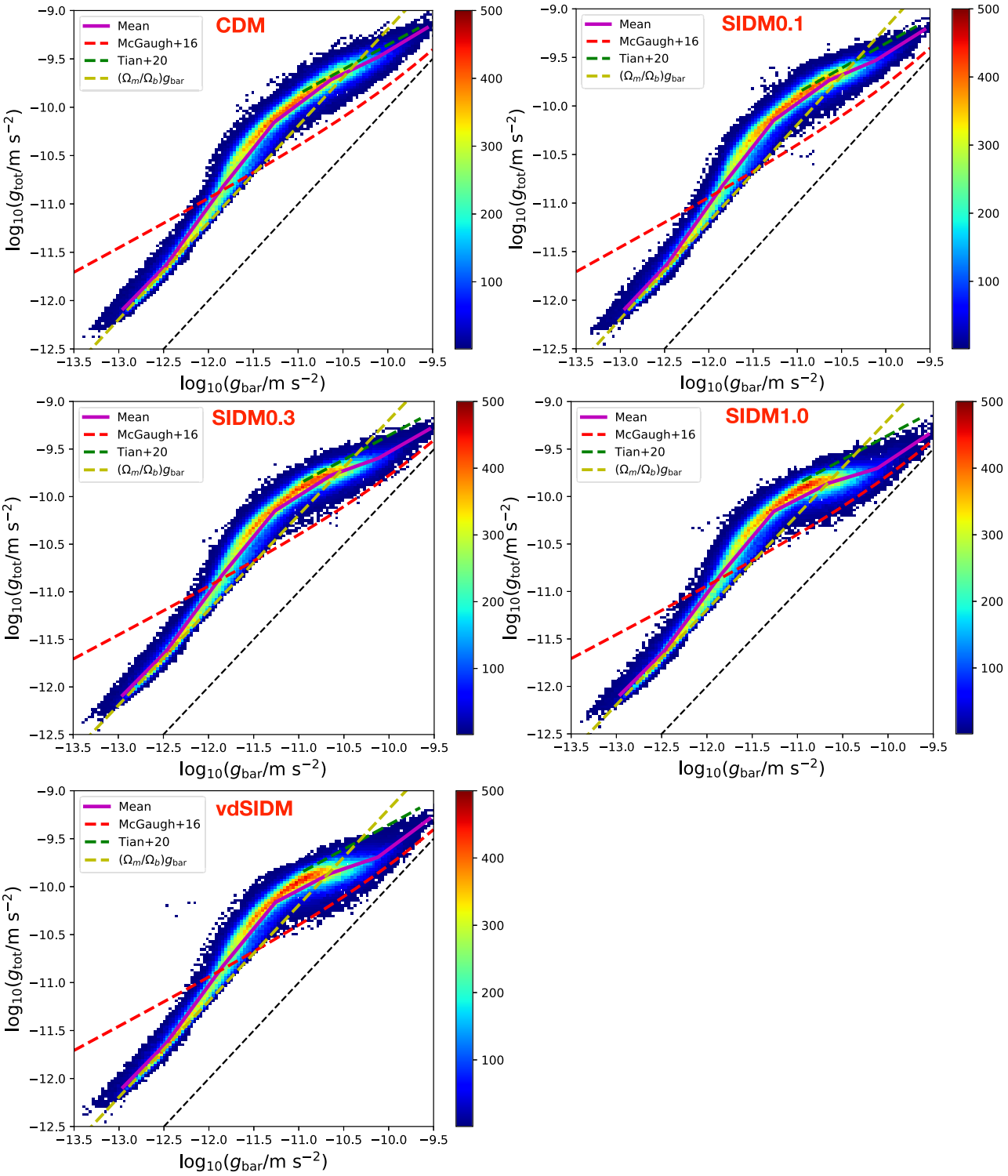

Figure 2. Histogram distribution of the baryonic and total centripetal accelerations ($g_{\rm bar}$, $g_{\rm tot}$) derived from the BAHAMAS halos at $z = 0.375$ with masses $E(z)$ $M_{200} > 5 \times 10^{13}\ M_{\odot}$. Each panel shows the results for a different dark matter model. The halo accelerations are logarithmically extracted at scales from $r = 15$ kpc to $r = 4000$ kpc. In each panel, the magenta solid line represents the mean $g_{\rm tot}$ as a function of $g_{\rm bar}$ for that simulation. The red dashed line shows the McGaugh et al. (2016) relation observed in spiral galaxies (see Equation (2)). The yellow dashed line shows the linear relationship $g_{\rm tot} = (\Omega_{\rm m}/\Omega_{\rm b})g_{\rm bar}$ corresponding to the cosmic ratio between total and baryonic mass densities. The green dashed line is the best-fit RAR observed for 20 high-mass galaxy clusters in the CLASH sample (Tian et al. 2020). The black dashed line shows the one-to-one relation.

for clusters at $z \gtrsim 0.1$. We recall that beyond $r \sim 100$ kpc, it is challenging to distinguish the CDM and SIDM models by measuring the mass density profile of galaxy clusters, as shown in Figure 1. The bottom left panel of Figure 4 shows that even beyond $r \sim 100$ kpc, the slope of the RAR for SIDM1.0 is shallower than that for CDM. Deviations in the RAR between CDM and SIDM are thus more significant than the conventional cusp–core features in the density profiles at larger radii.

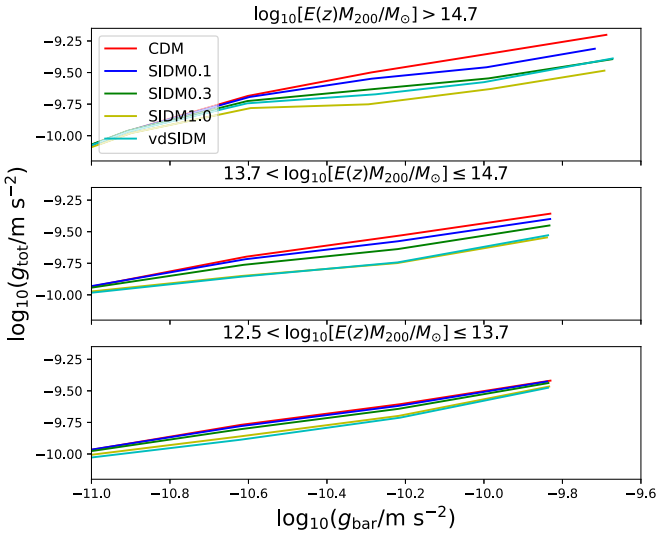

Figure 3. Comparison of the RARs for simulated halos in three different mass bins at $z = 0.375$. In each panel, the results are shown for our five different dark matter models. A minimum cutoff radius of $r_{\rm cut} = 15$ kpc is used (see Figure 4).

For the radial range of weak-lensing-only measurements, the discrepancy becomes tiny and would be almost impossible to detect. Hence, a combined strong- and weak-lensing analysis is typically required to distinguish SIDM and CDM in terms of the RAR, because this enables the measurement of the total enclosed mass down to and below approximately 100 kpc.

The key features used to distinguish different dark matter models are largely driven by information in the inner region of cluster halos. In Appendix A, we further investigate whether the correlation between the acceleration ratio $g_{\rm tot}/g_{\rm bar}$ and the clustercentric distance r, namely the $g_{\rm tot}/g_{\rm bar}$–r relation, can provide sufficient information to distinguish between different dark matter models. We find that the radial $g_{\rm tot}(r)/g_{\rm bar}(r)$ (or $M_{\rm tot}(r)/M_{\rm bar}(r)$) profiles of cluster halos derived from different dark matter runs of the BAHAMAS simulation significantly overlap with each other, even in their innermost region, and hence the $g_{\rm tot}/g_{\rm bar}$–r relation has a much weaker sensitivity to the SIDM cross section than the $g_{\rm tot}$–$g_{\rm bar}$ relation.

3.3. Power-law Characterization of the Cluster-scale RAR

We characterize the halo RARs obtained in Section 3.2, focusing on cluster halos in the highest-mass bin with $E(z)M_{200} > 5 \times 10^{14}\ M_{\odot}$ at $z = 0.375$. To this end, we assume a power-law function of the form

$$\log_{10}(g_{\rm tot}/{\rm m\ s^{-2}}) = b_1 \log_{10}(g_{\rm bar}/{\rm m\ s^{-2}}) + b_0, \qquad (7)$$

with b_1 the logarithmic slope and b_0 the intercept. At $g_{\rm bar} \sim 10^{-11}$ m s^{-2}, the mean cluster RARs for all the dark matter runs converge to a power law with $b_1 \approx 1.15$ and $b_0 \approx 2.68$ (see the top panel of Figure 3). Then, the logarithmic slope begins to flatten gradually at $g_{\rm bar} \gtrsim 10^{-11}$ m s^{-2}. At $g_{\rm bar} \gtrsim 10^{-10.6}$ m s^{-2}, the cluster RAR is found to be highly sensitive to the SIDM cross section.

In Table 1, we summarize the best-fit values of b_1 and b_0 for the CDM and four SIDM runs characterized in the high-acceleration regime $g_{\rm bar} > 10^{-10.6}$ m s^{-2}. It should be noted that we also fitted the mean RARs at $g_{\rm bar} > 10^{-10.6}$ m s^{-2} using the McGaugh et al. (2016) relation (Equation (2)), finding that only the CDM case can be well described by this functional form with an acceleration scale of $g_{\dagger} = (1.42 \pm 0.06) \times 10^{-9}$ m s^{-2}, which is much higher than the characteristic acceleration scale $g_{\dagger} \approx 1.2 \times 10^{-10}$ m s^{-2} observed at galaxy scales (Section 1).

Table 1 also lists the levels of intrinsic scatter $\Delta_{\rm int}$ around the mean relations obtained for the five different dark matter runs. In all cases, we find a remarkably tight distribution in $\log g_{\rm tot}$–$\log g_{\rm bar}$ space, with a slight increase in $\Delta_{\rm int}$ with increasing cross section. For the CDM, SIDM0.1, and SIDM0.3 models, the values of $\Delta_{\rm int}$ agree within the errors with $\Delta_{\rm int} = 0.064^{+0.013}_{-0.012}$ (in dex) determined for the CLASH sample (Tian et al. 2020).

3.4. Evolution of the Cluster-scale RAR

Here we investigate the evolution of the RAR by analyzing simulated halos at two redshifts, $z = 0$ and $z = 0.375$. For this purpose, we focus on massive cluster halos with $E(z)M_{200} > 5 \times 10^{14}\ M_{\odot}$ (Sections 3.2 and 3.3). At $z = 0$, we have a total of 82 cluster halos in this subsample.

Figure 5 shows the comparison of the cluster-scale RARs at $z = 0$ and $z = 0.375$. Compared to $z = 0.375$, we find a larger discrepancy at $z = 0$ between the CDM and SIDM results: the larger the scattering cross section, the lower the total acceleration at high $g_{\rm bar}$ (see also Section 3.2). The SIDM dependence increasing toward lower redshift is expected, because the radius out to which SIDM significantly affects density profiles is well described by the radius where there has been one scattering event per particle over the age of the halo (Robertson et al. 2021). This suggests that cluster RAR measurements for lower-z samples should provide a more sensitive test of the SIDM cross section. We find that the cluster RAR derived from vdSIDM at $z = 0$ resembles well that from SIDM0.3 at $z = 0$.

4. Comparison with Observational Data

In this section, we compare the cluster-scale RARs derived from the BAHAMAS simulations with observations of galaxy clusters. An observational determination of the cluster RAR relies on accurate measurements of both total and baryonic mass profiles, $M_{\rm tot}(< r)$ and $M_{\rm bar}(< r)$, for a sizable sample of galaxy clusters. The baryonic mass in galaxy clusters is dominated by the hot intracluster gas, except in their central region where the BCG dominates the total baryonic mass (e.g., Sartoris et al. 2020).[5] Thus, estimates of baryonic mass for both components are essential. Furthermore, unbiased estimates for the total mass in galaxy clusters are critical for a robust determination of the cluster RAR.

In this context, Tian et al. (2020) determined the RAR at BCG–cluster scales for a sample of 20 high-mass galaxy clusters targeted by the CLASH program, by combining weak and strong gravitational lensing data (Umetsu et al. 2014, 2016; Merten et al. 2015; Zitrin et al. 2015), X-ray gas mass measurements (Donahue et al. 2014), and estimates of BCG stellar mass. The contribution of stellar mass from member galaxies was statistically corrected for. To date, this is the only study that uses gravitational lensing data to directly probe the total acceleration $g_{\rm tot}$ in galaxy clusters. By contrast, other studies based on hydrostatic estimates for $g_{\rm tot}$ could potentially

[5] The mean effective (half-light) radius of the CLASH BCGs is $\langle R_{\rm e} \rangle \sim 30$ kpc (Tian et al. 2020).

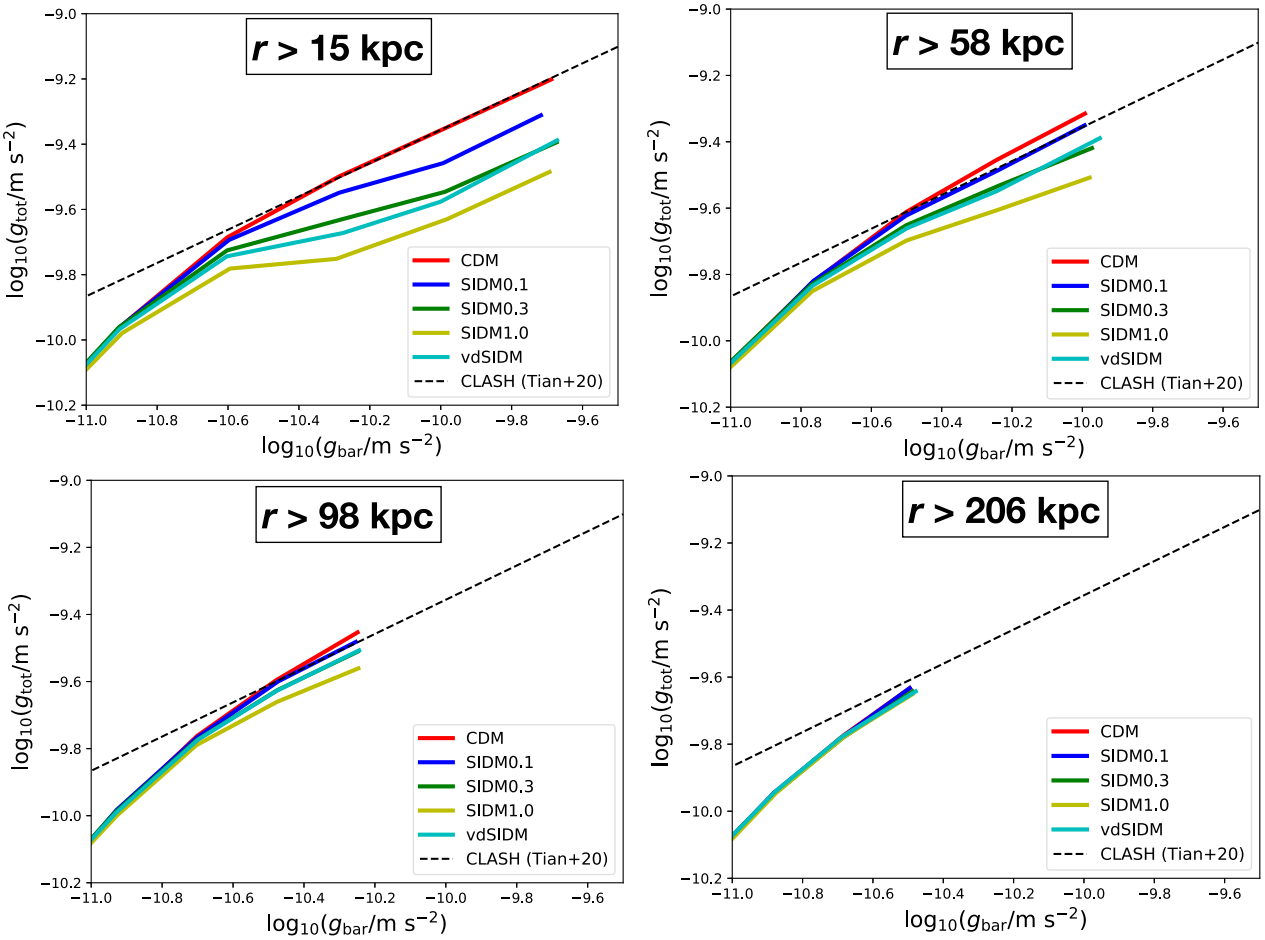

Figure 4. Dependence of the cluster-scale RAR on the inner radial cut. The four panels show the comparison of the RARs obtained with different radial cuts. Solid lines with different colors show the mean relations for different dark matter runs, derived for massive cluster halos with $E(z)M_{200} > 5 \times 10^{14}\ M_{\odot}$.

Table 1
Cluster-scale RAR and Its Intrinsic Scatter Characterized in the High-acceleration Regime

Dark Matter Model	b_1	b_0	$\Delta_{\rm int}$ (dex)
CDM	0.526	−4.096	0.064
SIDM0.1	0.422	−5.225	0.058
SIDM0.3	0.350	−6.025	0.076
SIDM1.0	0.334	−6.270	0.100
vdSIDM	0.379	−5.753	0.091

Note. For each model, the RAR is derived for a subsample of cluster halos at $z = 0.375$ with masses $E(z)M_{200} > 5 \times 10^{14}\ M_{\odot}$. A cutoff radius of $r_{\rm cut} = 15$ kpc is used. The quantities b_1 and b_0 represent the slope and intercept of the power-law fit (Equation (7)) in the high-acceleration region of $\log_{10}(g_{\rm bar}/{\rm m\ s^{-2}}) > -10.6$. The $\Delta_{\rm int}$ parameter is the intrinsic scatter in dex.

bias the true underlying RAR. In this study, we thus focus on the CLASH RAR studied by Tian et al. (2020).

4.1. CLASH Data

With the aim of precisely determining the mass profiles of galaxy clusters using deep 16-band imaging with the Hubble

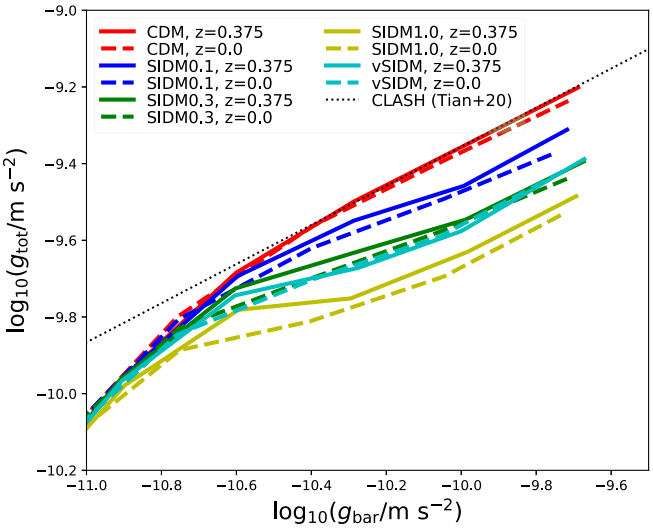

Figure 5. Comparison of the cluster-scale RARs between two different simulation snapshots, $z = 0.375$ (solid line) and $z = 0.0$ (dashed line), obtained for massive cluster halos with $E(z)M_{200} > 5 \times 10^{14}\ M_{\odot}$. The results are shown for five different dark matter runs. The dotted line shows the RAR derived for the CLASH sample at a median redshift of $\bar{z} = 0.377$ (Tian et al. 2020).

Space Telescope (HST; Postman et al. 2012) and ground-based weak-lensing observations (Umetsu et al. 2014), a subsample of 20 CLASH clusters was X-ray-selected to be massive (>5 keV), with nearly concentric X-ray isophotes and a well-defined X-ray peak located close to the BCG. For this subsample, no lensing information was used a priori to avoid a biased sample selection. Cosmological hydrodynamical simulations suggest that the CLASH X-ray-selected subsample is mostly composed of relaxed systems (∼70%) and largely free of orientation bias (Meneghetti et al. 2014). Another subsample of five clusters was selected by their exceptional lensing strength to magnify galaxies at high redshift. These clusters often turn out to be dynamically disturbed massive systems (Umetsu 2020).

The CLASH sample spans nearly an order of magnitude in mass, $5 \lesssim M_{200}/10^{14}\ M_\odot \lesssim 30$. For each of the 25 clusters, HST weak- and strong-lensing data products are available in their central regions (Zitrin et al. 2015). Umetsu et al. (2016) combined wide-field weak-lensing data obtained primarily with Suprime-Cam on the Subaru telescope (Umetsu et al. 2014) and the HST weak- and strong-lensing constraints of Zitrin et al. (2015). For an observational determination of the RAR, Tian et al. (2020) combined the X-ray data products from Donahue et al. (2014) and the lensing data products from Umetsu et al. (2016), yielding a subsample of 20 CLASH clusters composed of 16 X-ray-selected and four lensing-selected systems. We note that five clusters of the CLASH sample were not included in the joint weak- and strong-lensing analysis performed by Umetsu et al. (2016) because of the lack of usable wide-field weak-lensing data. Consequently, they were also excluded from our analysis.

The CLASH subsample analyzed by Tian et al. (2020) has a median redshift of $\bar{z} = 0.377$, which closely matches our simulation snapshot at $z = 0.375$. The typical resolution limit of the mass reconstruction set by the HST lensing data is 10″, which corresponds to ≈50 kpc at $\bar{z} = 0.377$ (Umetsu et al. 2016). It was found by Umetsu et al. (2016) that the stacked lensing signal of the CLASH X-ray-selected subsample is well described by a family of cuspy, sharply steepening density profiles, such as the Navarro–Frenk–White (hereafter NFW; Navarro et al. 1996, 1997), Einasto (Einasto 1965), and DARKexp (Hjorth & Williams 2010) profiles. Of these, the NFW model best describes the CLASH lensing data (see also Umetsu & Diemer 2017). In contrast, the single power-law, cored isothermal, and Burkert models are statistically disfavored by the averaged lensing profile having a pronounced radial curvature.

For each of the 20 clusters, Umetsu et al. (2016) performed a spherical NFW fit to the reconstructed projected mass density profile by accounting for all relevant sources of uncertainty, including measurement errors, cosmic noise due to the projection of large-scale structure uncorrelated with the cluster, statistical fluctuations of the projected cluster lensing signal due to halo triaxiality, and correlated substructures.

In this analysis, we use the CLASH RAR data set (Tian et al. 2020) published in Tian et al. (2020), which contains $N_{\rm data} = 84$ data points in $\log g_{\rm tot}$–$\log g_{\rm bar}$ space. Tian et al. (2020) extracted total and baryonic mass estimates where possible at $r = 100$, 200, 400, and 600 kpc. For each cluster, they also included a single constraint at $r \lesssim 30$ kpc in the central BCG region. These data points are sufficiently well separated from each other so as to avoid oversampling and reduce correlations between adjacent data points.

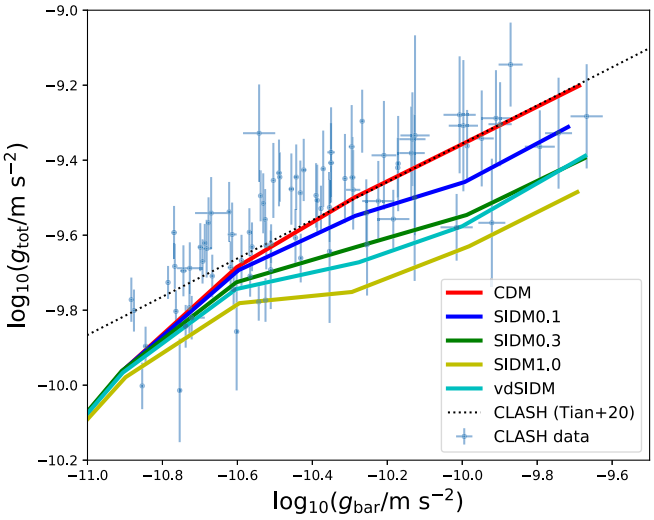

Figure 6. Comparison of the CLASH RAR (Tian et al. 2020) with our BAHAMAS predictions of the cluster-scale RAR at $z = 0.375$, derived from five different dark matter runs (thick colored lines). The CLASH measurements of cluster centripetal accelerations ($g_{\rm bar}$, $g_{\rm tot}$; Tian et al. 2020) are shown with blue points with error bars. The black dotted line shows the best-fit RAR for the CLASH sample at a median redshift of $\bar{z} = 0.377$.

The CLASH measurements of centripetal accelerations ($g_{\rm bar}$, $g_{\rm tot}$) are shown in Figure 6, along with our BAHAMAS predictions of the RAR for massive cluster halos with $E(z)M_{200} > 5 \times 10^{14}\ M_\odot$, derived from five different dark matter runs at $z = 0.375$. The best-fit CLASH RAR obtained by Tian et al. (2020) has $b_1 = 0.51^{+0.04}_{-0.05}$, $b_0 = -4.26^{+0.46}_{-0.47}$, and $\Delta_{\rm int} = 0.064^{+0.013}_{-0.012}$ dex, which are in excellent agreement with the best-fit RAR for the BAHAMAS-CDM run characterized in the high-acceleration region of $g_{\rm bar} > 10^{-10.6}$ m s^{-2} (Table 1).

4.2. Statistical Comparison

To make a quantitative comparison between the BAHAMAS simulations and the CLASH observations, we define the χ^2 function as

$$\chi^2 = \sum_{i=1}^{N_{\rm data}} \frac{(\log_{10} g_{{\rm tot},i} - \log_{10} \hat{g}_{{\rm tot},i})^2}{\Delta_i^2 + \Delta_{\rm int}^2}, \tag{8}$$

where i runs over all data points from the CLASH data set, $g_{{\rm tot},i}$ is the total acceleration at the ith data point, Δ_i is the measurement uncertainty, $\Delta_{\rm int} \approx 0.064$ is the intrinsic scatter for the CLASH sample determined by Tian et al. (2020), and $\hat{g}_{{\rm tot},i}$ is the theoretical prediction for the total acceleration at $g_{\rm bar} = g_{{\rm bar},i}$ from the BAHAMAS simulations. The resulting χ^2 values evaluated for different dark matter runs are listed in Table 2.

To statistically characterize the level of agreement between data and simulations, we use frequentist measures of statistical significance. Specifically, we use the chance probability of exceeding the observed χ^2 value to quantify the significance of the match for each dark matter run. For each case, we calculate the probability to exceed (PTE), or the right-tailed p value, for a given value of χ^2 assuming the standard χ^2 probability distribution function. We adopt a significance threshold of $\alpha = 0.05$ as the dividing line between satisfactory (PTE > 0.05) and unsatisfactory (PTE < 0.05) matches to the CLASH RAR data set. Since no optimization (or model fitting) is performed in our χ^2 evaluations, the number of degrees of freedom is

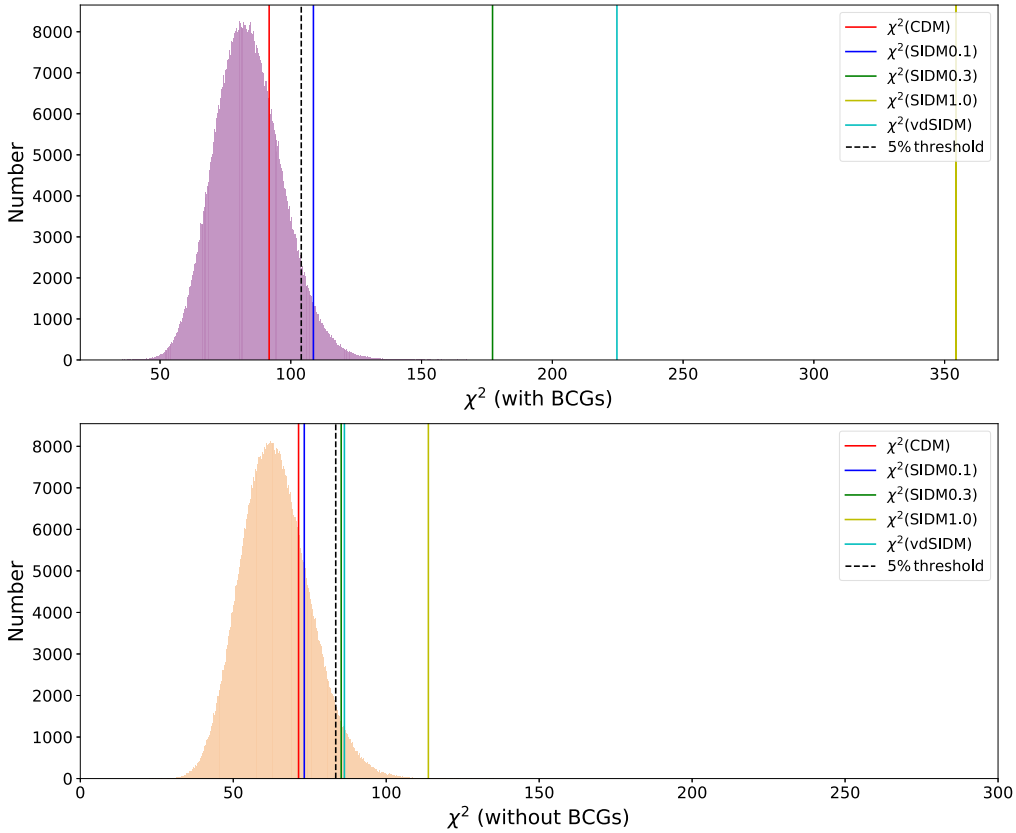

Figure 7. The χ^2 distribution of the CLASH RAR data set constructed from Monte Carlo simulations. Solid vertical lines indicate the observed χ^2 values for five different dark matter models. The black dashed vertical line corresponds to the significance threshold of $\alpha = 0.05$. The upper and lower panels show the results with and without including the central 100 kpc region, respectively.

Table 2
Summary of the χ^2 Test Using the $g_{\rm tot}$–$g_{\rm bar}$ Relation (RAR)

	With BCGs			Without BCGs		
	χ^2[a]	PTE[b]	Fraction[c]	χ^2 [a]	PTE[b]	Fraction[c]
CDM	91.7	0.264	0.264	71.3	0.246	0.246
SIDM0.1	108.6	0.037	0.036	73.2	0.200	0.200
SIDM0.3	177.1	1.3×10^{-8}	0.0	85.3	0.039	0.039
SIDM1.0	354.5	6.3×10^{-35}	0.0	113.8	1.3×10^{-5}	1.4×10^{-5}
vdSIDM	224.7	8.9×10^{-15}	0.0	86.3	0.033	0.033

Notes.
[a] Observed χ^2 value between the CLASH data and each dark matter model.
[b] Probability to exceed the observed χ^2 value assuming the standard χ^2 probability distribution function.
[c] Fraction of Monte Carlo realizations exceeding the observed value of χ^2.

$N_{\rm data} = 84$ in all cases. The resulting values of PTE for each dark matter run are listed in Table 2. We find that the CDM run (PTE = 0.264) gives a satisfactory match, whereas all the SIDM runs give unacceptable matches to the CLASH data. Among the SIDM runs, SIDM0.1 has a PTE of 0.036, which is close to but slightly below the adopted threshold.

As a consistency check, we perform Monte Carlo simulations to derive the χ^2 distribution expected from the measurement errors $\{\Delta_i\}_{i=1}^{N_{\rm data}}$ and the intrinsic scatter $\Delta_{\rm int}$ for the CLASH RAR. In each simulation, we construct a synthetic data set $\{g_{{\rm bar},i}^{\rm (MC)}, g_{{\rm tot},i}^{\rm (MC)}\}_{i=1}^{N_{\rm data}}$ by creating a Monte Carlo realization of random Gaussian noise $n_i \equiv \log_{10} g_{{\rm tot},i}^{\rm (MC)} - \log_{10} \widehat{g}_{{\rm tot},i} = \pm \sqrt{\Delta_i^2 + \Delta_{\rm int}^2}$ at $\log_{10} g_{{\rm bar},i}^{\rm (MC)} = \log_{10} g_{{\rm bar},i}^{\rm (CLASH)}$ and then calculate the value of $\chi^2 = \sum_i n_i^2/(\Delta_i^2 + \Delta_{\rm int}^2)$. We repeat this procedure 10^6 times to generate a large set of Monte Carlo realizations and obtain the distribution of χ^2 values. In Table 2, we list the fraction of Monte Carlo realizations exceeding the observed value of χ^2 for each dark matter run. In all cases, the Monte Carlo fraction exceeding the χ^2 value is precisely consistent with the PTE calculated with the standard χ^2 distribution function. In the upper panel of Figure 7, we compare the χ^2 distribution of the CLASH data set constructed from our Monte Carlo simulations with the observed χ^2 values for the CDM and four SIDM models. This figure gives a visual summary of the χ^2 test (Table 2).

We perform a likelihood-ratio test of SIDM models to quantify whether the inclusion of collisional features of dark matter is statistically warranted by the data. Velocity-independent SIDM models have one additional degree of

Table 3
Likelihood-ratio Test of the SIDM Models

	With BCGs		Without BCGs	
	$\Delta\chi^2$	Significance Level	$\Delta\chi^2$	Significance Level
SIDM0.1	16.9	4.1σ	1.9	1.4σ
SIDM0.3	85.4	9.2σ	14.0	3.8σ
SIDM1.0	262.8	16.2σ	42.5	6.8σ
vdSIDM	133.0	11.2σ	15.0	3.4σ

Note. The observed value of $\Delta\chi^2 = \chi^2 - \chi^2_{\rm CDM}$ relative to the CDM model is listed for each SIDM model explored in this work. The number of degrees of freedom for each comparison is one for all cases except vdSIDM with two degrees of freedom.

freedom relative to the CDM model. For vdSIDM, there are two additional degrees of freedom relative to the CDM model. These models are reduced to the CDM model in the limit of a vanishing cross section. Table 3 lists for each SIDM model the differences in the χ^2 value $\Delta\chi^2 = \chi^2 - \chi^2_{\rm CDM}$ relative to the CDM model and the corresponding significance level. Compared with the fiducial model of CDM, SIDM0.1 is disfavored at a significance level of 4.1σ.

These results are based on the CLASH RAR at BCG–cluster scales, which includes, for each cluster, a single constraint in the central BCG region at $r \lesssim 30$ kpc. However, since the typical resolution of CLASH mass reconstructions is $\Delta r \approx 50$ kpc (Section 4.1), the mass distribution is not resolved in the BCG region and thus the CLASH constraints on $g_{\rm tot}$ at the BCG scale are model dependent to some extent. Moreover, the distribution of baryonic and dark matter in cluster cores is sensitive to baryonic physics (e.g., Cui et al. 2018).

We therefore repeat the tests described above using core-excised RAR data. Excluding the central $r < 100$ kpc region from the CLASH data set, we have 64 data points at $r \in [100, 600]$ kpc. The results of the χ^2 test with the core-excised data set are summarized in Table 2. Of the five BAHAMAS dark matter runs, CDM and SIDM0.1 provide satisfactory matches to the core-excised CLASH RAR, at a significance level of $\alpha = 0.05$. Excluding the BCG regions results in a weaker but still competitive constraint on the SIDM cross section (Table 3). With a likelihood-ratio test, we find that the core-excised CLASH RAR data disfavor the SIDM0.3 model at the 3.8σ level with respect to the CDM model.

We note that in the above analysis, the measurement uncertainty of $\log_{10} g_{\rm bar}$ (which is typically $\sim$7% of that of $\log_{10} g_{\rm tot}$ and thus negligible in the analysis) is not taken into account. In Appendix B, we perform an alternative analysis in terms of the $g_{\rm tot}/g_{\rm bar}$–$g_{\rm bar}$ relation, which is referred to as the mass discrepancy–acceleration relation (MDAR; see Famaey & McGaugh 2012). In this MDAR analysis, we can explicitly account for the uncertainty in the $g_{\rm bar}$ measurements. We find that the inclusion of the measurement uncertainty in $g_{\rm bar}$ has only a minor impact on the statistical inference and does not change our conclusions regarding the acceptance of dark matter models.

5. Discussion

In this section, we first discuss current limitations and possible improvements of SIDM constraints from measurements of the cluster RAR. Then, we compare our results to previous astrophysical constraints on SIDM.

5.1. Possible Systematics and Improvements

In this work, we analyzed the CLASH RAR data set of Tian et al. (2020), which consists of $N_{\rm data} = 84$ data points ($g_{\rm bar}$, $g_{\rm tot}$) inferred from the multiwavelength CLASH observations of 20 high-mass galaxy clusters (Section 4.1). In Tian et al. (2020), the measurements of centripetal accelerations were sparsely sampled over a sufficiently wide range of clustercentric distances so as to reduce the covariance between adjacent data for each cluster. Thus, our comparison of the BAHAMAS simulations and CLASH measurements (Equation (8)) involves a two-step procedure, which ignores the covariance and does not fully exploit all the information contained in the data. As a result, our analysis is likely to overestimate the significance of our constraints. In principle, these limitations can be overcome by using a forward-modeling method. In particular, likelihood-free approaches based on forward simulations allow us to bypass the need for a direct evaluation of the likelihood function assuming Gaussian statistics, which avoids the complex derivation of the covariance matrix in an inherently complex problem (e.g., Tam et al. 2022).

Another potential source of systematic uncertainty is the smoothing of the inner density profile due to cluster miscentering (e.g., Johnston et al. 2007). Because of the CLASH selection, our cluster sample exhibits, on average, a small positional offset between the BCG and the X-ray peak, characterized by an rms offset of $\sim$40 kpc (Umetsu et al. 2014, 2016). This level of offset is comparable to the typical effective radius $R_{\rm e}$ of CLASH BCGs ($\langle R_{\rm e}\rangle \sim 30$ kpc; Section 4) but sufficiently small compared to the range of cluster radii of interest (say, $r \gtrsim 100$ kpc). Moreover, since the RAR method uses the same aperture to compare total and baryonic accelerations, the miscentering effect is not expected to significantly affect the SIDM constraint, although it could potentially contribute to the scatter in the RAR inferred from cluster observations.

The total and baryonic mass profiles of galaxy clusters, $M_{\rm tot}(< r)$ and $M_{\rm bar}(< r)$, inferred from observational data are model-dependent to some extent. Tian et al. (2020) found that the observed surface brightness distribution of CLASH BCGs is well described by a de Vaucouleurs profile, which is a special case of the Sérsic model, with a Sérsic index of $n = 4$. Accordingly, they modeled the 3D stellar mass distribution in the CLASH BCGs with a Hernquist profile, which closely resembles the de Vaucouleurs law in projection (Hernquist 1990; see their Figure 4), especially at $\gtrsim 0.5R/R_{\rm e}$ where Tian et al. (2020) extracted stellar mass estimates of the CLASH BCGs.

On the other hand, Tian et al. (2020) modeled the total mass distribution of CLASH clusters with an NFW profile, which best describes the stacked lensing profile of the CLASH sample (Umetsu et al. 2016; see Section 4.1). However, the choice of the cuspy NFW model implicitly assumes collisionless CDM, which could lead to a biased inference of the cluster RAR in an SIDM cosmology. In particular, this NFW assumption in our analysis is likely to underestimate the goodness of fit for the SIDM models. In future studies, it will thus be important to consider more flexible and self-consistent mass models, such as the density profiles of Einasto (1965) and Diemer & Kravtsov (2014), with an additional parameter to capture the radial curvature of the central density profile that depends on the SIDM cross section (Eckert et al. 2022b).

5.2. Comparison with Other Work

Self-interactions between dark matter particles are expected to make halos more spherical than triaxial halos of collisionless CDM, especially in the central region where the scattering rate is largest. Self-interactions in the optically thin regime also reduce the central dark matter densities, transforming a cusp into a core. Moreover, offsets between the galactic and dark-matter centroids in merging clusters can be used to constrain the SIDM cross section. Previous studies placed upper limits on the self-interaction cross section of dark matter particles using such observed density features in galaxy clusters (for a review, see Tulin & Yu 2018).

Peter et al. (2013) compared the halo ellipticities inferred from lensing and X-ray observations with cosmological simulations with SIDM cross sections of $\sigma/m = 0.03$, 0.1, and 1 $\mathrm{cm^2\,g^{-1}}$. They found that the strong-lensing measurement of the cluster ellipticity for MS 213723 (Miralda-Escudé 2002) is compatible with an SIDM cross section of $\sigma/m = 1$ $\mathrm{cm^2\,g^{-1}}$, whereas the X-ray shape measurement of the isolated elliptical galaxy NGC 720 (Buote et al. 2002) is consistent with $\sigma/m = 0.1$ $\mathrm{cm^2\,g^{-1}}$.

Using the galaxy–dark-matter offset measured in the moving subcluster of the Bullet Cluster, Randall et al. (2008) placed an upper limit of $\sigma/m < 1.25$ $\mathrm{cm^2\,g^{-1}}$ at the 68% confidence level (CL). Harvey et al. (2015) performed an ensemble analysis of offset measurements for 72 substructures in 30 systems, including both major and minor mergers, and set an upper limit of $\sigma/m < 0.47$ $\mathrm{cm^2\,g^{-1}}$ at the 95% CL. Wittman et al. (2018) revisited the analysis of Harvey et al. (2015) using more comprehensive data and carefully reinterpreted their refined offset measurements, finding that the SIDM constraint of Harvey et al. (2015) is relaxed to $\sigma/m \lesssim 2$ $\mathrm{cm^2\,g^{-1}}$.

Analyzing observations of X-rays and the SZ effect, Eckert et al. (2022b) constrained the structural parameters of the mass density profiles for a sample of 12 massive X-COP clusters, assuming that the intracluster gas is in hydrostatic equilibrium. They used the BAHAMAS-SIDM simulations to construct an empirical scaling relation between the Einasto shape parameter and the velocity-independent SIDM cross section. With this relation and the assumption of hydrostatic equilibrium, they obtained an upper limit of $\sigma/m < 0.19$ $\mathrm{cm^2\,g^{-1}}$ at the 95% CL.

In this study, we have obtained competitive constraints on the SIDM cross section using cluster RAR measurements. By comparing the CLASH RAR data set with the mean RARs derived from the BAHAMAS simulations, we are able to reject an SIDM model with $\sigma/m = 0.1$ $\mathrm{cm^2\,g^{-1}}$ at the 4.1σ CL with respect to the CDM model. Excluding the central $r < 100$ kpc region, we find that an SIDM model with $\sigma/m = 0.3$ $\mathrm{cm^2\,g^{-1}}$ is disfavored at the 3.8σ level with respect to CDM.

6. Summary and Conclusions

The RAR is a tight relation between the total and baryonic centripetal accelerations, $g_{\rm tot}$ and $g_{\rm bar}$, inferred for galaxies and galaxy clusters (McGaugh et al. 2016; Tian et al. 2020). This tight empirical correlation offers a new possibility of testing the collisionless nature of dark matter at galaxy–cluster scales.

As a first step toward this goal, we studied in this paper the RAR in simulated halos for both CDM and SIDM models, using the BAHAMAS suite of cosmological hydrodynamical simulations (McCarthy et al. 2017, 2018; Robertson et al. 2019). We analyzed simulations at $z = 0$ and $z = 0.375$ run with four different SIDM models (SIDM0.1, SIDM0.3, SIDM1.0, and vdSIDM; see Section 2), as well as collisionless CDM.

For each dark matter model, we have determined the mean $g_{\rm tot}$ as a function of $g_{\rm bar}$, or the halo RAR, in halos of different mass bins (Section 3; see Figure 2). We find that the slope of the halo RAR at high acceleration ($g_{\rm bar} \gtrsim 10^{-10.6}$ $\mathrm{m\,s^{-2}}$) decreases with increasing SIDM cross section. This flattening feature at high $g_{\rm bar}$ is more significant in more massive halos at lower redshift (Figures 3 and 5), consistent with the fact that the scattering rate is proportional to the local dark matter density and velocity dispersion (Equation (1)). This suggests that the high-$g_{\rm bar}$ cluster-scale RAR for low-redshift samples can be used to probe the nature of dark matter.

Focusing on massive cluster halos at $z = 0.375$, we have also characterized the slope (b_1), intercept (b_0), and intrinsic scatter ($\Delta_{\rm int}$) of the mean RAR at high $g_{\rm bar}$ for different dark matter models (see Table 1). In all cases, we find a remarkably tight distribution in $\log g_{\rm tot}$–$\log g_{\rm bar}$ space, with a slight increase in $\Delta_{\rm int}$ with increasing SIDM cross section. We find that only the CDM case can be well described by Equation (2) proposed by McGaugh et al. (2016), with an acceleration scale of $g_\dagger = (1.42 \pm 0.06) \times 10^{-9}$ $\mathrm{m\,s^{-2}}$. This is much higher than the characteristic acceleration scale of $g_\dagger \approx 1.2 \times 10^{-10}$ $\mathrm{m\,s^{-2}}$ observed at galaxy scales (McGaugh et al. 2016).

We have compared the halo RARs from the BAHAMAS-CDM and -SIDM runs to the cluster RAR inferred from CLASH observations (Section 4; see Tables 2 and 3). Our comparison shows that the RAR in the CDM model provides an excellent match to the CLASH RAR (Tian et al. 2020). This comparison includes the high-$g_{\rm bar}$ regime probed by the BCGs. By contrast, models with a larger SIDM cross section (hence with a greater flattening in $g_{\rm tot}$ at high $g_{\rm bar}$) yield increasingly poorer matches to the CLASH RAR. Excluding the BCG regions, we obtain a weaker but still competitive constraint on the SIDM cross section. Using the RAR data outside the central $r < 100$ kpc region, we find that an SIDM model with $\sigma/m = 0.3$ $\mathrm{cm^2\,g^{-1}}$ is disfavored at the 3.8σ level with respect to the CDM model. However, it should be noted that the choice of the NFW model used for fitting the CLASH lensing data (Tian et al. 2020) implicitly assumes collisionless CDM, which could lead to a biased inference of the cluster RAR in an SIDM cosmology. As a result, this NFW assumption is likely to underestimate the goodness of fit for the SIDM models. In future work, it will be important to use more flexible mass models with an additional parameter to describe the central density slope that depends on the SIDM cross section (Eckert et al. 2022b).

In this study, we have demonstrated the power and potential of the RAR for testing the collisionless nature of dark matter. Thus far, the cluster RAR has been determined using gravitational lensing only for the CLASH sample. To place stringent and robust constraints on the SIDM cross section, it is necessary to increase the sample of clusters for which lensing and X-ray observations are available over a broad radial range down to $r \sim 100$ kpc (Section 3.2). For nearby clusters at $z < 0.1$, such mass measurements can be obtained from wide-field weak-lensing observations (e.g., Okabe et al. 2014). For clusters at higher redshifts, combined strong and weak lensing is required to distinguish SIDM and CDM using the RAR. The ongoing CHEX-MATE project will provide such ideal

multiwavelength data sets of high quality, for a minimally biased, signal-to-noise-limited sample of 118 Planck galaxy clusters at $0.05 < z < 0.6$ detected through the SZ effect (CHEX-MATE Collaboration et al 2021). Extending this work to the CHEX-MATE sample will thus be a substantial step toward understanding the collisionless nature of dark matter.

Acknowledgments

We thank the anonymous referee for valuable comments that improved the clarity of the paper. We acknowledge fruitful discussions with Yong Tian, Teppei Okumura, and Stefano Ettori. This work is supported by the Ministry of Science and Technology of Taiwan (grant MOST 109-2112-M-001-018-MY3) and by the Academia Sinica Investigator award (grants AS-IA-107-M01 and AS-IA-112-M04). Parts of this research were carried out at the Jet Propulsion Laboratory, California Institute of Technology, under a contract with the National Aeronautics and Space Administration (80NM0018D0004).

Software: Astropy (Astropy Collaboration et al. 2018), matplotlib (Hunter 2007), NumPy (van der Walt et al. 2011), Python (Van Rossum & Drake 2009), Scipy (Virtanen et al. 2020).

Appendix A
Correlation between the Total and Baryonic Matter Distributions

The key features used to distinguish different dark matter models mainly come from the inner region of cluster halos ($r \lesssim 200$ kpc), as shown in Figure 4. Here, we further investigate whether the correlation between the acceleration ratio $g_{\rm tot}/g_{\rm bar}$ (or the total-to-baryonic mass ratio, $M_{\rm tot}/M_{\rm bar}$) and the clustercentric distance r can provide sufficient information to distinguish between different dark matter models.

The top panel of Figure 8 shows the mean and standard deviation profiles of $g_{\rm tot}(r)/g_{\rm bar}(r)$ as a function of cluster radius r, derived for each of the dark matter runs of the BAHAMAS simulation at $z = 0.375$ using the high-mass subsample with $E(z)M_{200} > 5 \times 10^{14}\ M_{\odot}$. The values of the logarithmic scatter of $g_{\rm tot}(r)/g_{\rm bar}(r)$ evaluated in the inner region of cluster halos ($r < 400$ kpc or $r < 200$ kpc) are listed in Table 4. The radial range of $r < 400$ kpc corresponds approximately to the high-acceleration region with $g_{\rm bar} > 10^{-10.6}$ m s^{-2} used to characterize the intrinsic scatter around the mean RAR, or the $g_{\rm bar}$–$g_{\rm tot}$ relation (Table 1).

Overall, the magnitude of the scatter in the $g_{\rm tot}/g_{\rm bar}$–r relation is about a factor of ∼1.6 larger than that of the RAR (see Table 1). As a result, the radial $g_{\rm tot}(r)/g_{\rm bar}(r)$ profiles of cluster halos derived from the different dark matter runs significantly overlap with each other, even in their innermost region (Figure 8). Therefore, we conclude that compared to the RAR or MDAR, the $g_{\rm tot}/g_{\rm bar}$–r relation (i.e., the $M_{\rm tot}(r)/M_{\rm bar}(r)$ profile) has a much weaker sensitivity to the SIDM cross section.

To understand the tightness of RAR/MDAR, we split the simulation data in $\log(g_{\rm tot}/g_{\rm bar})$–$\log g_{\rm bar}$ space into six different radial bins ranging from 15 to 1200 kpc and show them separately in the left panels of Figure 9. In each radial bin, the MDAR sequence spans a wide range in $g_{\rm bar}$, indicating that even dark matter particles at large clustercentric distances can contribute to the high-acceleration region. The distribution of $g_{\rm tot}/g_{\rm bar}$ in a given radial bin is obtained by projecting each set of color-coded data onto the y-axis in Figure 9, which results in a large scatter around the mean value $\langle g_{\rm tot}/g_{\rm bar}\rangle$. Therefore, the

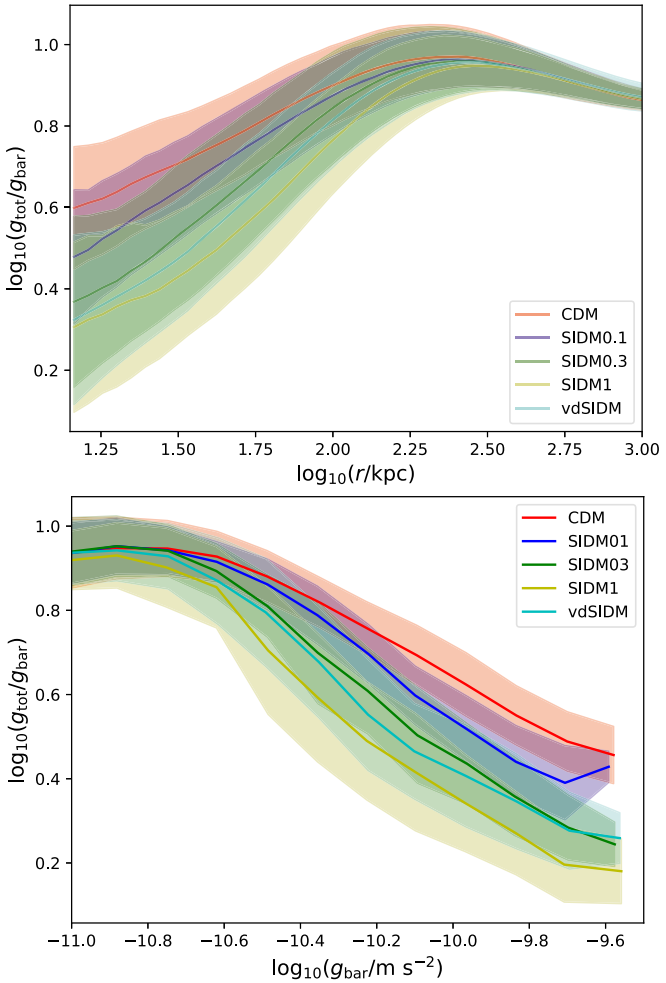

Figure 8. Ratio of the total acceleration $g_{\rm tot}$ to the baryonic acceleration $g_{\rm bar}$ as a function of cluster radius r (upper panel) and as a function of baryonic acceleration $g_{\rm bar}$ (lower panel) for massive cluster-scale halos with $E(z)M_{200} > 5 \times 10^{14}\ M_{\odot}$ at $z = 0.375$. The results are shown separately for five different dark matter simulation runs. For each dark matter model, the solid line represents the mean relation and the shaded area shows the standard deviation around the mean.

Table 4
Logarithmic Scatter around the Mean $g_{\rm tot}/g_{\rm bar}$–r Relation Evaluated in the Inner Region of Cluster-scale Halos

Dark matter model	σ (< 400 kpc) (dex)	σ (< 200 kpc) (dex)
CDM	0.104	0.111
SIDM0.1	0.104	0.113
SIDM0.3	0.141	0.156
SIDM1.0	0.138	0.154
vdSIDM	0.125	0.137

Note. For each model, the $g_{\rm tot}/g_{\rm bar}$–r relation is derived for a subsample of cluster halos at $z = 0.375$ with masses $E(z)M_{200} > 5 \times 10^{14}\ M_{\odot}$. An inner cutoff radius of $r_{\rm cut} = 15$ kpc is used.

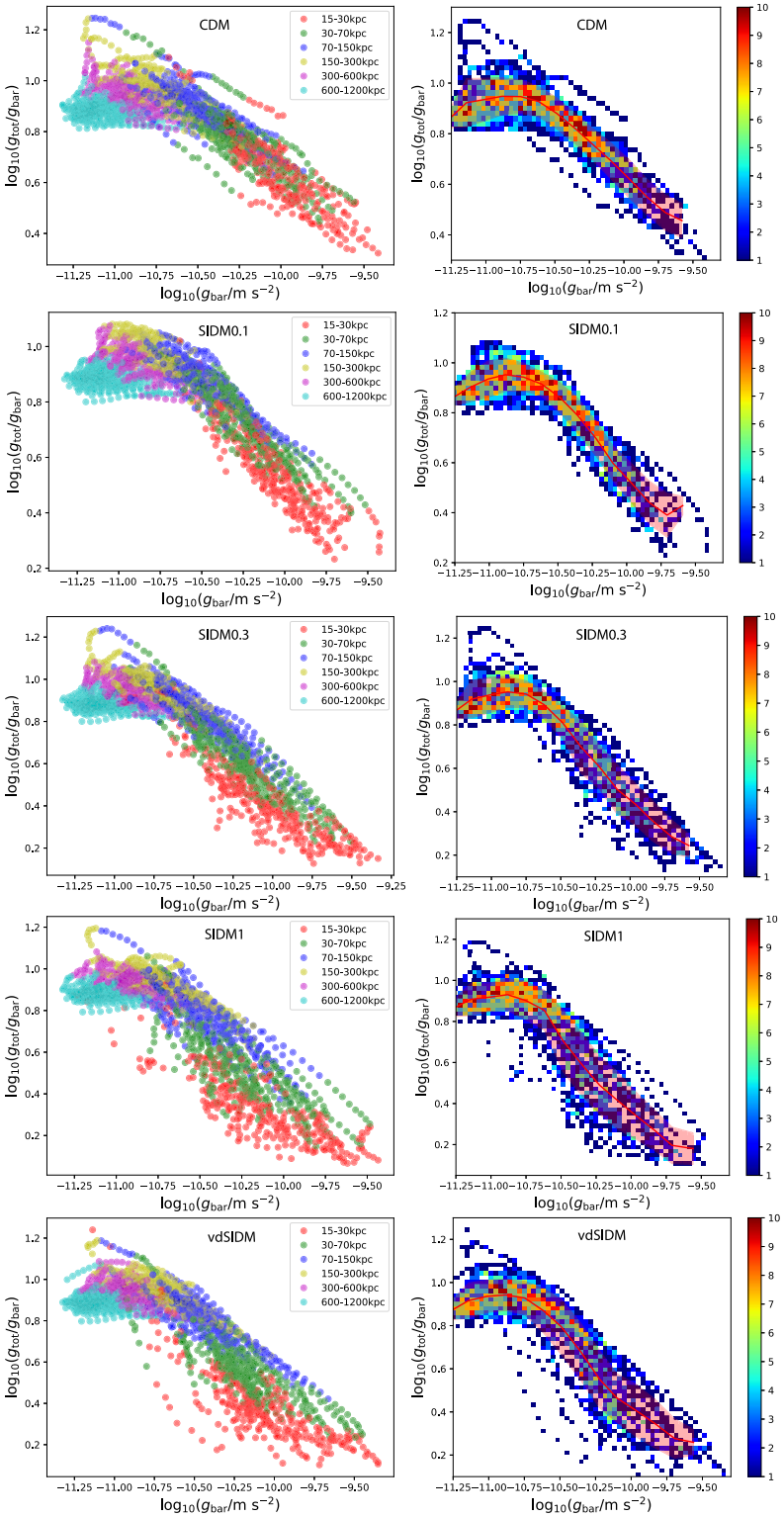

Figure 9. The $g_{\rm tot}/g_{\rm bar}$–$g_{\rm bar}$ diagram derived for a subsample of massive cluster-scale halos with $E(z)M_{200} > 5 \times 10^{14}\ M_{\odot}$ at $z = 0.375$. The results are shown separately for five different dark matter runs of the BAHAMAS simulation. In the left panels, the data are divided into six different radial bins ranging from $r = 15$ kpc to 1200 kpc. All points in each panel are color-coded according to their radial bin. In the right panels, the corresponding histogram distribution is shown for each dark matter run. In each panel, the red solid line represents the mean relation and the red shaded area shows the standard deviation around the mean relation.

tight correlation in the RAR/MDAR appears to be a unique signature of the empirical coupling between the total and baryonic components, which increases the ease of distinguishing between CDM and SIDM models.

The physical origin and the nature of this tight empirical coupling between the total and baryonic accelerations are still under debate. In the future, it will be useful to search for different combinations of the total and baryonic mass

properties of galaxy clusters to identify other low-scatter probes of the SIDM cross section.

Appendix B
Accounting for the Measurement Uncertainty of the Baryonic Acceleration

In this appendix, we explicitly account for the measurement uncertainty of $g_{\rm bar}$ in our analysis of the CLASH RAR data set. To this end, we utilize the MDAR, namely $g_{\rm tot}/g_{\rm bar}$ as a function of $g_{\rm bar}$, and follow the analysis procedure described in Section 4.2. The χ^2 function in this analysis is defined by

$$\chi^2 = \sum_{i=1}^{N_{\rm data}} \frac{[\log_{10}(g_{{\rm tot},i}/g_{{\rm bar},i}) - \log_{10}(\widehat{g}_{{\rm tot},i}/\widehat{g}_{{\rm bar},i})]^2}{\Delta_i^2 + \Delta_{\rm int}^2}, \quad \text{(B1)}$$

where i runs over all data points from the CLASH data set, $\Delta_i^2 = \Delta^2(\log_{10} g_{{\rm tot},i}) + \Delta^2(\log_{10} g_{{\rm bar},i})$ represents the total uncertainty including the measurement errors in both $\log_{10} g_{\rm bar}$ and $\log_{10} g_{\rm tot}$, and $\Delta_{\rm int}$ is the log-normal intrinsic scatter of $g_{\rm tot}$ at fixed $g_{\rm bar}$.

Figure 10 shows the distribution of the CLASH-MDAR data and the BAHAMAS predictions of the mean $g_{\rm tot}/g_{\rm bar}$–$g_{\rm bar}$ relation derived from five different dark matter runs. The resulting χ^2 values and corresponding PTE values evaluated for the respective dark matter runs are listed in Table 5.

When the central BCG constraint is included, only the CDM model gives a satisfactory match to the CLASH data set, which is consistent with the result of the RAR-based analysis given in Section 4.2. However, we note that the SIDM0.1 model now has a PTE value of 0.047, which is very close to but slightly below the significance threshold of $\alpha = 0.05$. When excluding the central BCG region of $r < 100$ kpc, we find that both CDM and SIDM0.1 provide satisfactory matches to the CLASH data. All these results are consistent with the findings based on the RAR analysis presented in Section 4.2, suggesting that the inclusion of the measurement uncertainty of $g_{\rm bar}$ has only a minor impact on the statistical inference and it does not change our conclusions of the accepted dark matter models.

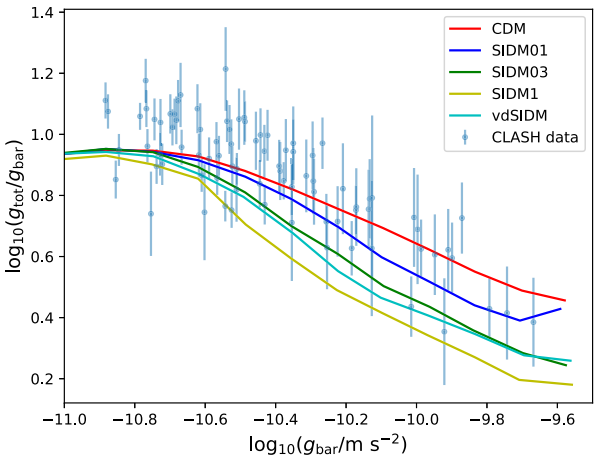

Figure 10. Comparison of the CLASH data with our BAHAMAS predictions of the cluster-scale $g_{\rm tot}/g_{\rm bar}$–$g_{\rm bar}$ relation at $z = 0.375$, derived from five different dark matter runs (thick colored lines). The CLASH measurements are shown with blue points with error bars.

Table 5
Summary of the χ^2 Test Using the $g_{\rm tot}/g_{\rm bar}$–$g_{\rm bar}$ Relation (MDAR)

	With BCGs		Without BCGs	
	χ^{2a}	PTE[b]	χ^{2a}	PTE[b]
CDM	89.32	0.314	70.18	0.278
SIDM0.1	106.8	0.047	73.46	0.221
SIDM0.3	177.4	1.2×10^{-8}	85.89	0.035
SIDM1.0	348.5	0.0	112.9	1.6×10^{-4}
vdSIDM	221.0	2.9×10^{-14}	83.65	0.031

Notes.
[a] Observed χ^2 value between the CLASH data and each dark matter model.
[b] Probability to exceed the observed χ^2 value assuming the standard χ^2 probability distribution function.

ORCID iDs

Sut-Ieng Tam https://orcid.org/0000-0002-6724-833X
Keiichi Umetsu https://orcid.org/0000-0002-7196-4822

References

Astropy Collaboration, Price-Whelan, A. M., Sipőcz, B. M., et al. 2018, AJ, 156, 123
Brouwer, M. M., Oman, K. A., Valentijn, E. A., et al. 2021, A&A, 650, A113
Buote, D. A., Jeltema, T. E., Canizares, C. R., & Garmire, G. P. 2002, ApJ, 577, 183
Chae, K.-H., Bernardi, M., Sheth, R. K., & Gong, I.-T. 2019, ApJ, 877, 18
Chan, M. H., & Del Popolo, A. 2020, MNRAS, 492, 5865
CHEX-MATE Collaboration, Arnaud, M., Ettori, S., et al. 2021, A&A, 650, A104
Cui, W., Knebe, A., Yepes, G., et al. 2018, MNRAS, 480, 2898
Davis, M., Efstathiou, G., Frenk, C. S., & White, S. D. M. 1985, ApJ, 292, 371
Diemer, B., & Kravtsov, A. V. 2014, ApJ, 789, 1
Donahue, M., Voit, G. M., Mahdavi, A., et al. 2014, ApJ, 794, 136
Dutton, A. A., Macciò, A. V., Obreja, A., & Buck, T. 2019, MNRAS, 485, 1886
Eckert, D., Ettori, S., Pointecouteau, E., van der Burg, R. F. J., & Loubser, S. I. 2022a, A&A, 662, 30
Eckert, D., Ettori, S., Robertson, A., et al. 2022b, A&A, 666, A41
Einasto, J. 1965, TrAlm, 5, 87
Famaey, B., & McGaugh, S. S. 2012, LRR, 15, 10
Flores, R. A., & Primack, J. R. 1994, ApJL, 427, L1
Garaldi, E., Romano-Díaz, E., Porciani, C., & Pawlowski, M. S. 2018, PhRvL, 120, 261301
Gopika, K., & Desai, S. 2021, PDU, 33, 100874
Harvey, D., Massey, R., Kitching, T., Taylor, A., & Tittley, E. 2015, Sci, 347, 1462
Harvey, D., Robertson, A., Massey, R., & McCarthy, I. G. 2019, MNRAS, 488, 1572
Hernquist, L. 1990, ApJ, 356, 359
Hinshaw, G., Larson, D., Komatsu, E., et al. 2013, ApJS, 208, 19
Hjorth, J., & Williams, L. L. R. 2010, ApJ, 722, 851
Hodson, A. O., & Zhao, H. 2017, A&A, 598, A127
Hunter, J. D. 2007, CSE, 9, 90
Jauzac, M., Eckert, D., Schwinn, J., et al. 2016, MNRAS, 463, 3876
Johnston, D. E., Sheldon, E. S., Tasitsiomi, A., et al. 2007, ApJ, 656, 27
Kaplinghat, M., Tulin, S., & Yu, H.-B. 2016, PhRvL, 116, 041302
Keller, B. W., & Wadsley, J. W. 2017, ApJL, 835, L17
Lelli, F., McGaugh, S. S., Schombert, J. M., & Pawlowski, M. S. 2017, ApJ, 836, 152
Ludlow, A. D., Benítez-Llambay, A., Schaller, M., et al. 2017, PhRvL, 118, 161103
Massey, R., Harvey, D., Liesenborgs, J., et al. 2018, MNRAS, 477, 669
McCarthy, I. G., Bird, S., Schaye, J., et al. 2018, MNRAS, 476, 2999
McCarthy, I. G., Schaye, J., Bird, S., & Le Brun, A. M. C. 2017, MNRAS, 465, 2936
McGaugh, S. S. 2004, ApJ, 609, 652
McGaugh, S. S., Lelli, F., & Schombert, J. M. 2016, PhRvL, 117, 201101
Meneghetti, M., Davoli, G., Bergamini, P., et al. 2020, Sci, 369, 1347
Meneghetti, M., Rasia, E., Vega, J., et al. 2014, ApJ, 797, 34

Merten, J., Meneghetti, M., Postman, M., et al. 2015, ApJ, 806, 4
Milgrom, M. 1983, ApJ, 270, 365
Miralda-Escudé, J. 2002, ApJ, 564, 1019
Moore, B. 1994, Natur, 370, 629
Navarro, J. F., Frenk, C. S., & White, S. D. M. 1996, ApJ, 462, 563
Navarro, J. F., Frenk, C. S., & White, S. D. M. 1997, ApJ, 490, 493
Okabe, N., Futamase, T., Kajisawa, M., & Kuroshima, R. 2014, ApJ, 784, 90
Oman, K. A., Brouwer, M. M., Ludlow, A. D., & Navarro, J. F. 2020, arXiv:2006.06700
Paranjape, A., & Sheth, R. K. 2021, MNRAS, 507, 632
Peter, A. H. G., Rocha, M., Bullock, J. S., & Kaplinghat, M. 2013, MNRAS, 430, 105
Postman, M., Coe, D., Benítez, N., et al. 2012, ApJS, 199, 25
Pradyumna, S., & Desai, S. 2021, PDU, 33, 100854
Pradyumna, S., Gupta, S., Seeram, S., & Desai, S. 2021, PDU, 31, 100765
Randall, S. W., Markevitch, M., Clowe, D., Gonzalez, A. H., & Bradač, M. 2008, ApJ, 679, 1173
Robertson, A., Harvey, D., Massey, R., et al. 2019, MNRAS, 488, 3646
Robertson, A., Massey, R., & Eke, V. 2017, MNRAS, 467, 4719
Robertson, A., Massey, R., Eke, V., Schaye, J., & Theuns, T. 2021, MNRAS, 501, 4610
Rocha, M., Peter, A. H. G., Bullock, J. S., et al. 2013, MNRAS, 430, 81
Rong, Y., Li, H., Wang, J., et al. 2018, MNRAS, 477, 230
Sartoris, B., Biviano, A., Rosati, P., et al. 2020, A&A, 637, A34
Spergel, D. N., & Steinhardt, P. J. 2000, PhRvL, 84, 3760
Tam, S.-I., Jauzac, M., Massey, R., et al. 2020, MNRAS, 496, 4032
Tam, S.-I., Umetsu, K., & Amara, A. 2022, ApJ, 925, 145
Tian, Y., Umetsu, K., Ko, C.-M., Donahue, M., & Chiu, I. N. 2020, ApJ, 896, 70
Tulin, S., & Yu, H.-B. 2018, PhR, 730, 1
Umetsu, K. 2020, A&ARv, 28, 7
Umetsu, K., & Diemer, B. 2017, ApJ, 836, 231
Umetsu, K., Medezinski, E., Nonino, M., et al. 2014, ApJ, 795, 163
Umetsu, K., Sereno, M., Tam, S.-I., et al. 2018, ApJ, 860, 104
Umetsu, K., Zitrin, A., Gruen, D., et al. 2016, ApJ, 821, 116
van der Walt, S., Colbert, S. C., & Varoquaux, G. 2011, CSE, 13, 22
Van Rossum, G., & Drake, F. L. 2009, Python 3 Reference Manual (Scotts Valley, CA: CreateSpace)
Vikhlinin, A., Kravtsov, A., Forman, W., et al. 2006, ApJ, 640, 691
Virtanen, P., Gommers, R., Oliphant, T. E., et al. 2020, NatMe, 17, 261
Wittman, D., Golovich, N., & Dawson, W. A. 2018, ApJ, 869, 104
Zhao, H., & Famaey, B. 2012, PhRvD, 86, 067301
Zitrin, A., Fabris, A., Merten, J., et al. 2015, ApJ, 801, 44